



## Efficient behaviour of hematite towards the photocatalytic degradation of NO<sub>x</sub> gases



R. Sugrañez <sup>a</sup>, J. Balbuena <sup>a</sup>, M. Cruz-Yusta <sup>a</sup>, F. Martín <sup>b</sup>, J. Morales <sup>a</sup>, L. Sánchez <sup>a,\*</sup>

<sup>a</sup> Departamento de Química Inorgánica, Facultad de Ciencias, Universidad de Córdoba, Campus de Rabanales, Edificio Marie Curie, 14071 Córdoba, Spain

<sup>b</sup> Departamento de Ingeniería Química, Facultad de Ciencias, Universidad de Málaga, Campus de Teatinos, 29071 Málaga, Spain

### ARTICLE INFO

#### Article history:

Received 20 August 2014

Received in revised form 9 October 2014

Accepted 10 October 2014

Available online 18 October 2014

#### Keywords:

Photocatalytic oxidation

Nitrogen oxides

Iron oxide

### ABSTRACT

Hematite,  $\alpha$ -Fe<sub>2</sub>O<sub>3</sub>, has been proven as a new visible photocatalyst towards the decontamination of NO<sub>x</sub> gases. Three samples were studied: NH (nanometric), RFH-A and RFH-B. The micronic RFH samples were obtained by using resorcinol–formaldehyde (RF) as a template. All samples constituted of only the  $\alpha$ -Fe<sub>2</sub>O<sub>3</sub> iron oxide phase, as revealed by X-ray diffraction, X-ray photoelectron spectroscopy and Raman techniques. The pyrolysis of RF is the reason for the presence of residual carbon in 0.9 and 3.5% of RFH-A and RFH-B samples, respectively. Photochemical oxidation (PCO) is proposed, implying the participation of  $\alpha$ -Fe<sub>2</sub>O<sub>3</sub>. The NO → NO<sub>2</sub> → NO<sub>3</sub><sup>−</sup> PCO process means the oxidation of NO and NO<sub>2</sub> toxic gases and their retention as HNO<sub>2</sub>/NO<sub>3</sub><sup>−</sup>. For the first time, this De-NO<sub>x</sub> mechanism is validated for hematite, with the adsorbed products (NO<sub>3</sub><sup>−</sup>) identified by infrared spectroscopy. The poor photocatalytic efficiency found with the use of pure hematite, the NH sample, is surpassed through the preparation of C-hematite compounds. Efficient behaviour is observed in this photocatalytic process for the RFH samples, exhibiting total NO<sub>x</sub> removal efficiency values as high as 17%.

© 2014 Elsevier B.V. All rights reserved.

### 1. Introduction

Atmospheric pollution has been recognised as one of the most serious environmental problems, causing a major concern for modern society. Large cities are among the areas with higher pollution emissions. Among the most common air pollutants, emitted mainly by traffic, are nitrogen oxides (NO<sub>x</sub> = NO + NO<sub>2</sub>) and volatile organic compounds (VOCs). Unfortunately, several adverse and harmful effects are associated with the presence of NO<sub>x</sub> in the atmosphere: (i) human health is affected in several ways when the amount of NO<sub>x</sub> interacting with lung tissues increases: emphysemas, bronchitis, etc.; (ii) together with sulfur oxides, NO<sub>x</sub> contributes towards the generation of acid rain. Even though intense regulations have been declared by the USA and Europe communities in order to limit the presence of NO<sub>x</sub> in the atmosphere, the recommended maximum amount of breathable NO<sub>x</sub> in working and urban atmospheres is usually surpassed in the centre of the big cities [1,2].

It is important to find ways to promote the NO<sub>x</sub> removal from the atmosphere. The use of photochemical oxidation (PCO)-assisted processes has gained great attention by researchers in

order to facilitate the degradation of inorganic toxic gases and organic pollutants. In addition, the PCO of NO<sub>x</sub> emissions has become a valid and simple technology over the past ten years, as confirmed by the large number of reports produced [2–9]. By using TiO<sub>2</sub>, as an efficient photocatalyst, NO<sub>x</sub> oxidation is easily promoted with only the participation of atmospheric oxygen, water and UV-A radiation [10]. According to this, new building materials incorporating a TiO<sub>2</sub> additive (De-NO<sub>x</sub> materials) are now commercialised as a new tool to combat NO<sub>x</sub> pollution in our cities [6,11–17]. However, samples used in cities like Madrid and Barcelona—with these types of products—have not yielded the expected results when trying to decontaminate NO<sub>x</sub> gases [18]. One of the drawbacks of TiO<sub>2</sub> as a photocatalyst is its poor ability to absorb sunlight. There is no doubt about the excellent performance of TiO<sub>2</sub> as a photocatalyst, but its photocatalytic activity only occurs with UV light of wavelengths shorter than 387 nm, owing to its band-gap of 3.2 eV, which allows us to take advantage of just 4–5% of the energy from sunlight [19,20]. As a consequence the photocatalytic performance of De-NO<sub>x</sub> materials using TiO<sub>2</sub> in dark areas of the cities, shadows of buildings or narrow streets in which there is no direct sunlight, dramatically decreases. Moreover, the performance of these materials will also be lessened in the cities of Central/Northern Europe or North America in which, owing to geography and gloomy weather conditions, only low levels of UV radiation reach to the surface [21].

\* Corresponding author. Tel.: +34 957 218620; fax: +34 957 218621.

E-mail address: [luis.sanchez@uco.es](mailto:luis.sanchez@uco.es) (L. Sánchez).

Accordingly, in recent years, the research community has begun to devote attention to the study of visible-light photocatalytic materials for this application. Nowadays, this interesting area of research is emerging and only a few materials have been reported:  $\text{Bi}_2\text{WO}_6$ ,  $\text{BiOBr}$ ,  $\text{Bi}_2\text{Mo}_3\text{O}_{12}$ ,  $\text{InVO}_4$ ,  $\text{In}(\text{OH})_x\text{S}_y$ ,  $\text{SrTiO}_3$ ,  $\text{N-TiO}_2$ ,  $\text{N,S-TiO}_2$ ,  $\text{Au-TiO}_2$  and  $\text{PtO}_x\text{-TiO}_2$  [22–31]. Bearing in mind that the future implementation of De- $\text{NO}_x$  materials in our cities would be a large-scale operation, the lowest cost materials must be considered. In this sense, we focused our attention on the study of iron oxide, because its abundance, environmentally benign nature and chemical stability make it attractive for use in practical photochemical applications. Increased interest has been found for the study of the hematite phase ( $\alpha\text{-Fe}_2\text{O}_3$ ), which is the most stable iron oxide with n-type semiconducting properties under ambient conditions, exhibiting a 1.9–2.2 eV band gap to absorb visible light [32], for which outstanding photocatalytic performances have been found through the preparation of nanoarchitectures [33–36]. To the best of our knowledge, the study of  $\text{Fe}_2\text{O}_3$  for De- $\text{NO}_x$  reactions is restricted to its use as slight load in UV-light photocatalysts— $\text{SrTiO}_3$  and  $\text{N-TiO}_2$  [27,28]—with the aim of expanding the photocatalytic action towards visible-light irradiation. The first evidence of the photochemical ability of hematite towards De- $\text{NO}_x$  reactions was pointed out by our group. Thus, transformed wastes or  $\text{TiO}_2$ -based building materials enriched with iron oxides showed an enhanced behaviour towards the photochemical degradation of  $\text{NO}_x$  gases [37]. Conversely, nanostructured  $\alpha\text{-Fe}_2\text{O}_3$  films evidenced the potential ability to photocatalytically oxidise  $\text{NO}$  gas [38].

This work studies the use of hematite,  $\alpha\text{-Fe}_2\text{O}_3$ , as a photocatalytic material for the capture and oxidation of  $\text{NO}_x$  gases, for the first time. In the other hand, it is known that incorporation of carbon content into the matrix of semiconductors enhance their photoactivity [39,40]. On this sense, previous works using carbon to increase the efficiency of  $\text{TiO}_2$  as a De- $\text{NO}_x$  photocatalyst were reported [8,41]. Following this strategy, carbon-enriched samples were prepared using inexpensive  $\text{Fe}^{3+}$  salt as a raw material and the resorcinol–formaldehyde (RF) polymer as a carbon source. The chemical, physical and optical properties of the samples were characterised, with the photochemical oxidation properties and capture of  $\text{NO}_x$  gases explained in terms of the specific characteristics of each sample.

## 2. Materials and methods

### 2.1. Preparation of nano-hematite and C-hematite composites

The nano- $\alpha\text{-Fe}_2\text{O}_3$  powders (NH sample) were obtained by using commercial nano- $\text{Fe}_2\text{O}_3$  maghemite phase as precursor [ $<50$  nm, iron(III) oxide, Aldrich]. The transformation of maghemite to hematite was carried out through calcination of the precursor sample at  $600^\circ\text{C}$  for 4 h. As expected, from the particle size of maghemite sample precursor [42], the  $\alpha\text{-Fe}_2\text{O}_3$  powders preserved the nanometric nature (particle size  $<100$  nm).

The RF polymer has been previously used with success as a chelating agent in the preparation of transition-metal oxides, with and without carbon content [43,44]. Herein, the C-Hematite compounds were obtained by using the RF polymer as a template, following the methodology reported by Kijima [45]. The reagents were all used as-received and included resorcinol (R, 99%, Aldrich), formaldehyde (F, formaldehyde 37%, methanol 8%, Aldrich), cetyltrimethylammonium bromide (CTAB, Aldrich), 1,3,5-trichlorobenzene (TCB, 98%, Aldrich), sodium hydroxide (NaOH, 96%, Aldrich), hydrochloric acid (HCl, 37%, Aldrich), iron(III) chloride 6-hydrate ( $\text{FeCl}_3 \cdot \text{H}_2\text{O}$ , Panreac) and ethanol (99.5%, Aldrich). In a typical preparation run, an aqueous solution of F (4.2 mL) was added drop-wise to a mixed solution of R (3.00 g), CTAB (5.0 g),

NaOH (0.14 g), TCB (1.73 mL) and  $\text{H}_2\text{O}$  (90 mL) at  $50^\circ\text{C}$  under continuous stirring to ensure complete dissolution of all chemicals. Moreover, 25.0 or 1.5 g of  $\text{FeCl}_3 \cdot 6\text{H}_2\text{O}$  was added to the solution with the aim to obtain an iron based RF polymer with final RF/Fe molar ratios of 1/4 (sample RFH-A) or 4/1 (sample RFH-B), respectively. Experiments made with other different RF/Fe ratios conducted to undesired results: negligible carbon content and/or the presence of iron oxide phases different to hematite. The mixtures were heated at  $90^\circ\text{C}$  for 24 h. In order to eliminate the excess of reagents [45] a portion (1 g) of the RF polymer– $\text{FeCl}_3$  composite was treated with 37 wt% HCl (1 mL) and ethanol (40 mL) under vigorous stirring at room temperature for 4 h. The solid was then filtered, washed with ethanol, dried at  $60^\circ\text{C}$  for 24 h and, after this time, heated to  $900^\circ\text{C}$  at a rate of  $12.5^\circ\text{C min}^{-1}$  and kept at this temperature level in air atmosphere for 10 h.

### 2.2. Instrumentation

The identification of crystalline phases was achieved using X-ray diffraction (XRD) on a Siemens D5000 X-ray diffractometer with  $\text{CuK}\alpha_{1,2}$  radiation. Scanning electron microscopy (SEM) images were obtained with a Jeol JMS-6400 microscope. Diffuse reflectance (DR) spectra were recorded at a scan rate of  $30\text{ nm min}^{-1}$  from 300 to 900 nm in 0.5 nm steps, using a Varian Cary 1E spectrophotometer. The modified DR absorption spectra were obtained by using the Kubelka–Munk function,  $F(R) = (1 - R)^2/(2R)$ .

Nitrogen absorption isotherms were obtained at  $77.4\text{ K}$  on an ASAP 2020 instrument from Micromeritics. Samples were degassed at  $105^\circ\text{C}$  for 3 h. Specific surface areas were calculated from  $\text{N}_2$  sorption isotherms, using the multipoint Brunauer–Emmett–Teller (BET) method. Infrared (IR) spectra were obtained with a Perkin–Elmer FTIR System Spectrum BX. The carbon content was analysed with the Dumas method, which is based on the combustion of the whole sample in an oxygen-enriched atmosphere at a high temperature in order to ensure complete combustion. An EuroVector Elemental Analyser EA3000 equipped with Callidus software (EuroVector SpA, Milan, Italy) was used.

X-ray photoelectron spectra (XPS) were recorded using non-monochromated  $\text{MgK}\alpha$  radiation ( $h\nu = 1253.6\text{ eV}$ ) and a hemispherical analyser operating at a constant pass energy of  $29.35\text{ eV}$  (Physical Electronics PHI 5700 spectrometer). Spectra were recorded with the X-ray generator operating at  $15\text{ kV}$  and  $300\text{ W}$ . The pressure in the analysis chamber was about  $10^{-7}\text{ Pa}$ . Binding energies were corrected against that for C 1s peak of adventitious carbon (and the methyl group) fixed at  $284.8\text{ eV}$ , before etching with  $4\text{ KeV Ar}^+$  ions, and for O 1s at  $530\text{ eV}$ , as recommended by Yamashita and Hayes [46]. Samples were mounted on a holder without adhesive tape and kept under high vacuum in the preparation chamber overnight prior to transfer to the spectrometer analysis chamber. Survey spectra over the range  $0\text{--}1100\text{ eV}$  were recorded at a  $187.85\text{ eV}$  pass energy, with each region being scanned several times to ensure an adequate signal-to-noise ratio. Spectra were recorded after each minute of Ar etching. Spectral data were processed by PHI-ESCA V8.0c and Multipack V9.3 software, both from Physical Electronics. High-resolution spectra were fitted after Shirley background correction, and XPS atomic concentrations were calculated from Fe 2p, Fe 3p, O 1s and C 1s photoelectron peak areas, using Shirley background subtraction and sensitivity factors supplied by the spectrometer manufacturer (PHI).

Raman spectra were recorded with a combined dispersive Raman spectrometer (SENTERRA) and a confocal microscope (Olympus BX series) equipped with a Nd:YAG laser (532, 633 and 785 nm) and a charge-coupled device detector. The spectra were registered using 785 nm and powers of 1 and  $10\text{ mW}$ . The 785 nm excitation was selected to avoid sample degradation due to the carbon content. For this purpose it is convenient to excite with

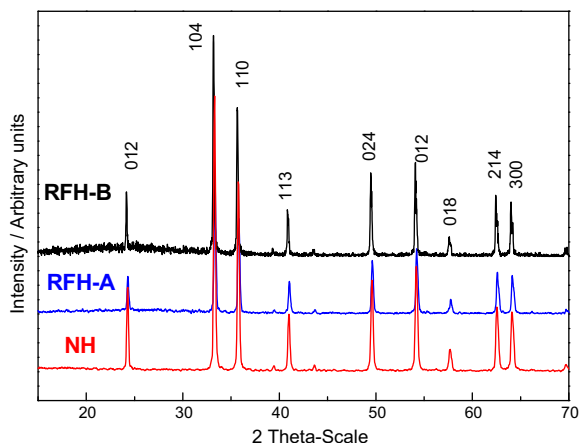


**Fig. 1.** XRD patterns of the NH, RFH-A and RFH-B samples.

less energetic wavelengths and a non-absorbing region of the UV–Vis spectrum. Simultaneously, the 785 nm excitation allows the minimisation of the fluorescence from the carbon content.

### 2.3. Photocatalysis

The photocatalytic activity of the materials towards the oxidation of NO was studied using a protocol similar to the standardised test method developed for the characterisation of air-purification performance, ISO 22197-1 [47]. However, some of the specifications described in this standard were modified in order to obtain better performance with the samples of this study. Thus, the tests were carried out on a 50 mm × 50 mm sampler holder placed in a laminar flow reactor. The reactor was placed inside a light sealed irradiation box (Solarbox 3000e RH) equipped with a Xe lamp with controlled irradiance. A 300 mg sample was used in each test and irradiated with artificial sunlight (25 and 580 W m<sup>-2</sup>, which are UV and visible irradiances, respectively). Air was conveyed by a gas-washing bottle, filled with demineralised water in order to keep the relative humidity of the supplied gas fixed at 50 ± 5%. Air and NO gas streams were mixed to obtain the desired concentration (100 ppb NO) and then sent in to the photoreactor. The accurate measurement of the concentration of NO, NO<sub>x</sub> and NO<sub>2</sub> was carried out using a chemiluminescence analyser (model Environnement AC32M); a flow rate, Q, of 0.30 L min<sup>-1</sup> was employed. Fig. S1 shows a schematic representation of the continuous flow gas photocatalytic reactor. For each test, the air/NO gas stream ran over the sample in the dark for a period of 10 min without changes in the NO<sub>x</sub> concentration profiles were observed, discarding the NO<sub>x</sub> adsorption on the sample surface or its direct photolysis. Subsequently, the photoreactor was irradiated for 30 min. The removal rate (%) of NO was defined according to the following equation:

$$\text{NO removal rate (\%)} = \frac{[\text{NO}]_{\text{inlet}} - [\text{NO}]_{\text{outlet}}}{[\text{NO}]_{\text{inlet}}} \times 100$$

where [NO]<sub>inlet</sub> represents the concentration of NO in the feed stream and [NO]<sub>outlet</sub> is the concentration of NO in the outlet stream.

## 3. Results and discussion

### 3.1. Samples characterisation

In this study, attention was devoted to the preparation of iron (III) oxide materials of the hematite phase, with different morphological features and carbon contents. Fig. 1 shows the XRD patterns

collected from the three samples studied: NH, RFH-A and RFH-B. For these specimens, all detected peaks were ascribable to the *hkl* reflections of rhombohedral α-Fe<sub>2</sub>O<sub>3</sub> (hematite) [PDF card No. 00-033-0664]. Interestingly, the RFH-B specimen showed a slight increase of the background signal intensity in the 2θ = 15–35° range, as a broad and low intense signal. This could be attributed to the presence of a considerable amount of amorphous carbon. In fact, the residual carbon from the pyrolysis of the RF polymer [43], when calcined at the same temperature under a nitrogen atmosphere, exhibits an XRD pattern similar to those reported for amorphous carbon compounds [48], with the presence of a broad and intense signal in the same 2θ range; see Fig. S2. This evidence is in agreement with the fact that the RFH-B sample presented a higher amount of carbon in its composition. Thus, the carbon contents measured were 0.9 and 3.5% for the RFH-A and RFH-B samples, respectively, and the value was negligible in the case of the NH sample. However, it is clear that the C content in the RFH samples increased with the RF/Fe ratio used in the synthesis.

Large differences were found in the morphology of these samples; see Fig. 2. The SEM images show that the NH sample maintained the nanometric nature of the commercial maghemite precursor, appearing as agglomerates of round nanoparticles of 70–110 nm in size (Fig. 2a and b). Conversely, the use of RF as a template modified the particle size and organisation. When a low RF/Fe ratio (1/4) was used in the synthesis (HRF-A sample), a framework composed of self-assembled flakes with large rounded particles of a micronic size (1–2 μm) is observed (Fig. 2c and d). However, by increasing the RF/Fe ratio up to 4 agglomerates of independent micronic particles appeared which were smaller in size (0.7–1.5 μm; Fig. 2e and f). As the SEM images revealed, no high specific-surface-area values are expected from these type of structures, as they have dense agglomerates of nanoparticles (NH), compact microstructures (HRF-A) or micronic particles (HRF-B). In fact, the BET surface areas measured were 5.1, 0.4 and 0.9 m<sup>2</sup> g<sup>-1</sup> for samples NH, HRF-A and HRF-B, respectively. In the case of the NH sample, the value obtained is similar to that previously reported for α-Fe<sub>2</sub>O<sub>3</sub> nanopowders [49].

The chemical composition of the iron oxide samples was confirmed through the study of their corresponding XPS and Raman spectra. The XPS spectra obtained for the RFH-B sample (representative of the three samples studied) is shown in Fig. 3. The spectrum of the Fe 2p region exhibits broad 2p<sub>1/2</sub> and 2p<sub>3/2</sub> signals, which are useful to identify, according to their binding energies, the presence of different iron oxidation states in the sample. The 2p<sub>3/2</sub> peaks for Fe<sup>3+</sup> and Fe<sup>2+</sup> are expected at 711.6 and 709.7 eV, respectively [50,51]. The observed positions were at 711.3 and 725 eV, which correspond to that reported for 2p<sub>1/2</sub> and 2p<sub>3/2</sub> signals, respectively, of Fe<sup>3+</sup> in Fe<sub>2</sub>O<sub>3</sub> [46]. The presence and position of the shake-up satellite pattern of the Fe 2p region is also sensitive to the oxidation state and can be used to distinguish between both iron valences. As expected for Fe<sub>2</sub>O<sub>3</sub>, the satellite signal appeared 8 eV higher than the main Fe 2p<sub>3/2</sub> peak (719.2 eV), whereas a signal at around 715 eV would be expected for the existence of Fe<sup>2+</sup> [46,52]. Moreover, it has been reported that no Fe 2p<sub>3/2</sub> satellite peak is observed for Fe<sub>3</sub>O<sub>4</sub> [46,53,54]. Nevertheless the presence of satellites in the 2p region makes deconvolution difficult; thus, it is advisable to also analyse the Fe 3p region. The Fe 3p XPS region, Fig. 3b, shows only one main peak at 55.6 eV, owing to the fact that the XPS spectrometer does not have the resolution to resolve the 3p<sub>3/2</sub> and 3p<sub>1/2</sub> peaks. The presence of Fe<sup>3+</sup> was again corroborated by deconvolution of the 3p region, which was carried out considering the Fe 3p<sub>3/2</sub> peak at 55.6 eV, a constant full width half maximum of 2.0, a 3p<sub>1/2</sub>/3p<sub>3/2</sub> peak-area ratio of 0.5 [55], and the fact that no signal was observed at the binding-energy value expected for Fe<sup>2+</sup>, that is, at 53.7 eV. Fig. 3c and d shows the C 1s and O 1s regions, respectively, after 1 min Ar<sup>+</sup> etching, for the RFH-B sample. The persistence of the C

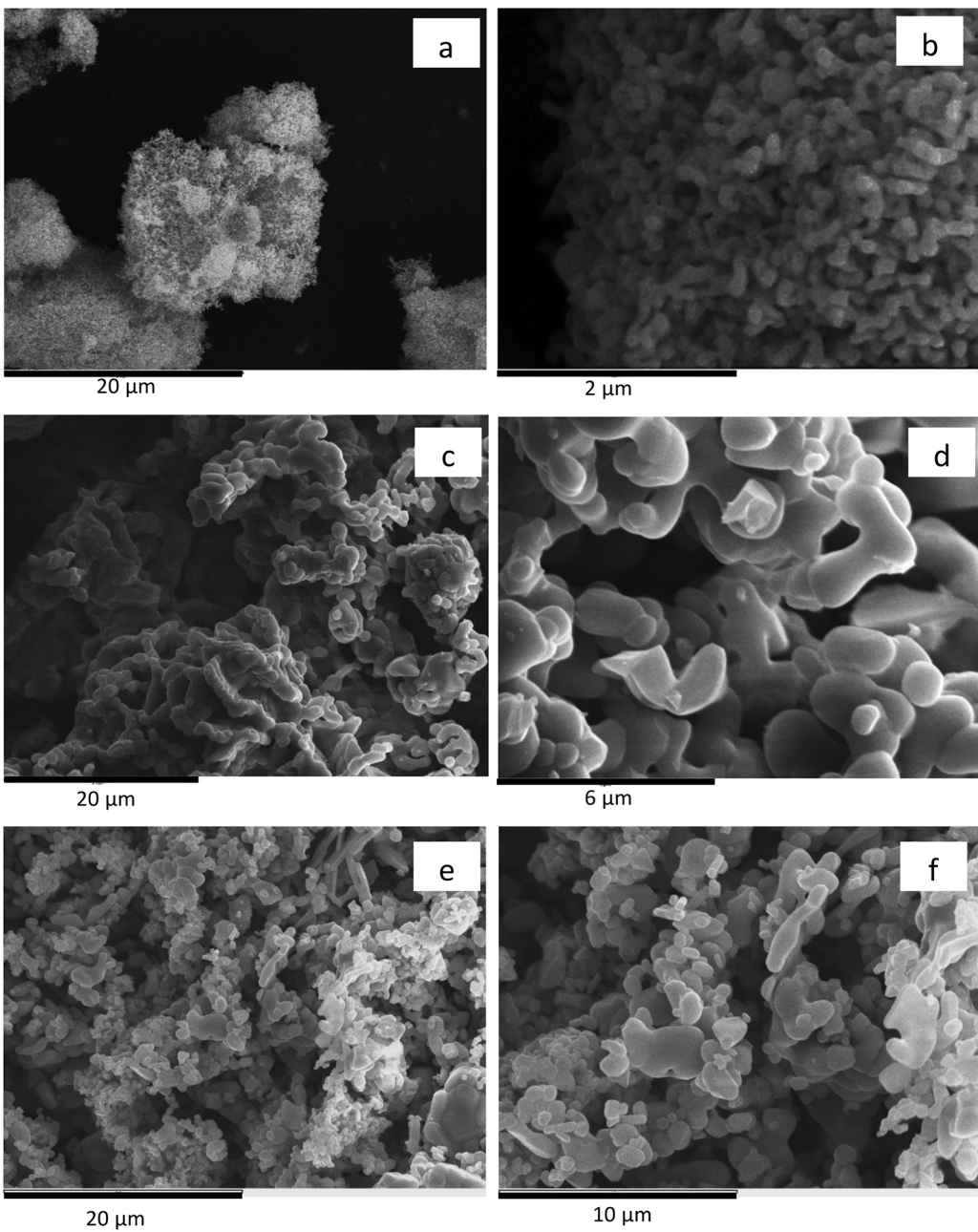


**Fig. 2.** Typical SEM images of (a and b) NH, (c and d) RFH-A and (e and f) RFH-B samples.

1s signal after etching is indicative of the carbon presence in the sample, confirming the chemical analysis results.

Additionally, the Raman spectra of the three samples are shown in Fig. S3. It is known that goethite ( $\alpha\text{-FeOOH}$ ) and lepidocrocite ( $\gamma\text{-FeOOH}$ ) are strongly Raman scattering, whereas magnetite ( $\text{Fe}_3\text{O}_4$ ) and, especially, maghemite ( $\gamma\text{-Fe}_2\text{O}_3$ ) are relatively weak Raman scatterers. However, owing to the existence of structural differences between their Raman spectra, the presence of hematite ( $\alpha\text{-Fe}_2\text{O}_3$ )—another strong scatterer—can be easily distinguished. The seven expected optical modes of even symmetry ( $2A_{1g} + 5E_g$ ) for the Raman spectrum of  $\alpha\text{-Fe}_2\text{O}_3$  were observed in the spectra of the three samples. In the case of the NH sample, these modes were located at 226 and 496 ( $A_{1g}$ ), as well as 245, 293, 299, 411 and  $612\text{ cm}^{-1}$  ( $E_g$ ). Even though the small peak at  $660\text{ cm}^{-1}$  could be assigned to magnetite inclusions, owing to the fact that  $\text{Fe}_3\text{O}_4$  has a strong Raman band at  $660\text{ cm}^{-1}$  [56], this has also been reported

in a number of characterisation studies of hematite. These studies consider this band as a characteristic of the hematite being related to the existence of a large number of defects in the hematite, in particular in surface and grain-boundary disorders [57,58]. The Raman peak intensity correlates with the crystallite size. The asymmetric line at  $290\text{--}298\text{ cm}^{-1}$  is usually reported as a doublet of  $E_{1g}$  symmetry and cannot easily be resolved [59]. The inset in Fig. S3 shows the deconvolution of this doublet for the NH sample. No other peaks were detected, indicating that the samples are  $\alpha\text{-Fe}_2\text{O}_3$  and free from other iron oxides or oxyhydroxides phases. Fig. S3 also shows a shift in the peak positions, corresponding to the seven optical modes in the Raman spectra of the RFH-A and RFH-B samples, varying from sample to sample and being more evident than in the NH sample. This shift in the peak positions could be due to differences in the chemical composition and, to some degree, could be dependent on variations in crystallinity,

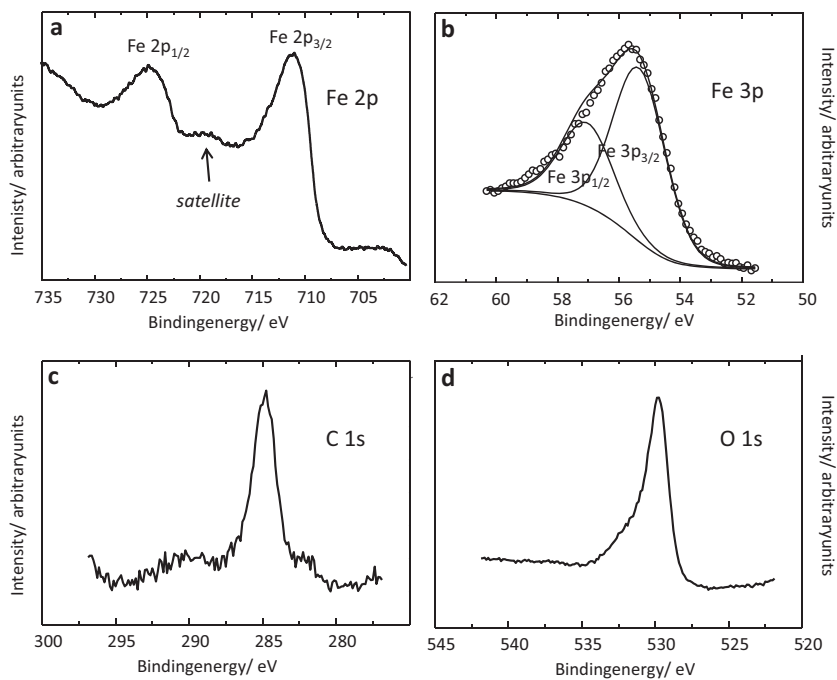


**Fig. 3.** XPS spectra obtained from RFH-B sample surface after 1 min etching with Ar<sup>+</sup>: (a) Fe 2p, (b) deconvolution of Fe 3p, (c) C 1s and (d) O 1s regions.

grain size and morphology. As mentioned above, an important difference between these samples is the carbon content.

The optical properties of the target iron-oxide materials were analysed by UV/Vis—near IR absorption spectroscopy. Fig. 4 reports optical spectra in the 400–900 nm visible-light range. The measured spectral shapes agreed, to a good extent, with those previously reported for  $\alpha$ -Fe<sub>2</sub>O<sub>3</sub> oxide [32,60]. Three main signals appears in the visible range at 575, 650 and 860 nm, which can be assigned to the  $^6A_{1g} \rightarrow ^4A_{1g}$ ,  $^6A_{1g} \rightarrow ^4T_{2g}$  and  $^6A_{1g} \rightarrow ^4T_{1g}$  transitions that are typical of the octahedral Fe<sup>3+</sup> ion in hematite [61]. The presence of carbon decreased, as the band intensity decreased throughout the absorption range. The acquired diffuse reflectance spectra have been converted to Kubelka-Munk function by  $F(R) = (1 - R)^2/(2R)$ . As  $F(R)$  is proportional to the absorption coefficient, the absorption coefficient in Tauc's equation can be substituted by  $F(R)$ , therefore Tauc's equation transforms in  $(h\nu F(R))^n = A(h\nu - E_g)$ , being  $n=2$  for direct allowed transition,  $A$  is a constant,  $h$  is Planck's constant and  $\nu$  the frequency. By fitting linear some points around the inflection point and extrapolating to intercept the  $h\nu$  axe (we have done this numerically) we found that the band gaps is 2.1 eV for the hematite (NH), which agrees

with it is expected for the bulk Fe<sub>2</sub>O<sub>3</sub>. The band gap reduces as the carbon content is increased,  $E_g = 2.0$  and  $E_g = 1.9$  eV for RFH-A and RFH-B, respectively. Fig. S4 shows (a) the  $(h\nu F(R))^n$  and (b) the first derivative versus  $h\nu$  plots for NH and RFH-A samples.

### 3.2. NO<sub>x</sub> photocatalytic oxidation test

Subsequently, attention was devoted to the photocatalytic degradation of NO in order to demonstrate the potential application of hematite in air purification. Fig. 5a shows the nitric oxide (NO), nitrogen dioxide (NO<sub>2</sub>) and total oxide (NO<sub>x</sub>=NO+NO<sub>2</sub>) concentration profiles obtained during the NO oxidation test under UV-Vis light irradiation. These profiles are characterised by three common stages. (i) The absence of UV-Vis light irradiation, as neither activation of the  $\alpha$ -Fe<sub>2</sub>O<sub>3</sub> sites nor NO oxidation took place. The concentration of NO was kept constant at 100 ppb during the first 10 min. (ii) Under UV-Vis light irradiation, the heterogeneous photocatalytic reaction took place and the oxidation of the pollutant began. The decrease in NO concentration reached its maximum (around 12.5%) and became constant in this period of time, indicating complete activation of the  $\alpha$ -Fe<sub>2</sub>O<sub>3</sub> sites. (iii) During the last 10 min of the test, when the irradiation was off, the NO concentration returned to its initial value. The photochemical process can be explained as follows: as the Fe<sub>2</sub>O<sub>3</sub> particles are irradiated by UV-Vis light irradiation, an electron in the valence band (VB) acquires the energy of a photon to become a photogenerated electron ( $e^-$ ), which migrates to the conduction band (CB) and simultaneously leaves behind a photogenerated hole ( $h^+$ ), as shown in Reaction (1). The pair of mobile charges produced can reach the surface of the semiconductor particle and initiate the redox process. On the Fe<sub>2</sub>O<sub>3</sub> particle surface, the H<sub>2</sub>O molecule reacts with  $h^+$  to produce a hydroxyl radical [62,63], Reaction (2). Subsequently, the hydroxyl radicals (OH<sup>•</sup>) lead to the oxidation of NO to NO<sub>2</sub>, which, in turn, produces nitrite and nitrate ions, Reactions (3)–(5). Moreover, the photoexcited electron in the conduction band can react with oxygen to form superoxide radical and this reactive oxygen specie (ROS) can participate in the final oxidation of NO<sub>x</sub> to nitrate ions, Reactions (6) and (7).

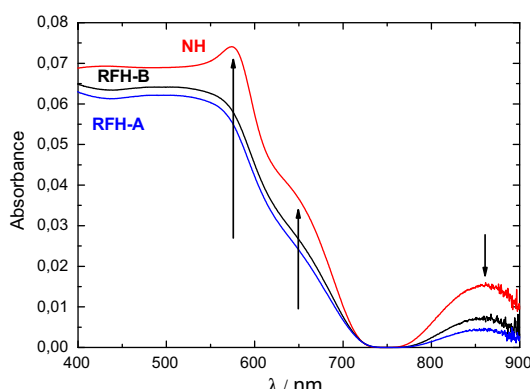


**Fig. 4.** The absorption spectra for NH, RFH-A and RFH-B samples.

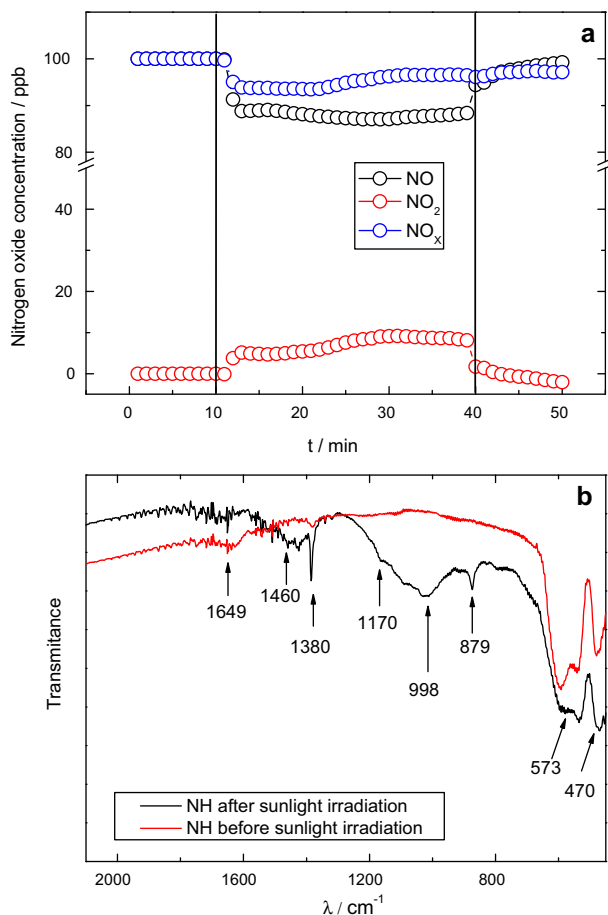


**Fig. 5.** (a) Nitrogen oxide concentration profiles obtained during the photochemical degradation of NO gas, under UV–Vis light irradiation, over the NH sample. (b) IR spectra of the NH sample before and after the NO<sub>x</sub> degradation test.

[17,23,64]. Even though the photocatalytic activity decreased with time, owing to the accumulation of nitrite/nitrate compounds on surface, this kind of slight deactivation could be easily regenerated by washing the photocatalyst with water [23,65].



To gain more of an insight into the photocatalytic reaction mechanism, IR spectra of the NH sample, before and after irradiation, were measured to investigate the presence of adsorbed products; Fig. 5b. Before irradiation (in the dark), no bands concerning N–O vibration modes were detected. The low intensity band at 1649 cm<sup>-1</sup> corresponds to the existence of large numbers of residual hydroxyl groups, which imply the O–H vibrating mode of traces of adsorbed water. Conversely, the intense bands at lower frequencies, 573 and 470 cm<sup>-1</sup>, could be attributed to Fe–O vibration modes of α-Fe<sub>2</sub>O<sub>3</sub> [49]. New bands in the 800–1500 cm<sup>-1</sup> range appear in the spectra obtained after irradiation. The bands located at 879, 998, 1170 and 1380 cm<sup>-1</sup> correspond to the stretching vibrations of NO<sub>3</sub><sup>-</sup>, and the low intensity and broad band at 1460 cm<sup>-1</sup>

can be ascribed to monodentate nitrite (–ONO<sup>-</sup>) [25,66,67], confirming that photocatalytic oxidation of NO took place.

As NO<sub>2</sub> is more toxic than NO [68], the photocatalyst performance should be evaluated by the total NO<sub>x</sub> removal. From Fig. 5a, it is observed that an important amount of NO<sub>2</sub> is released during the irradiation of the sample. Thus, around half of the NO molecules follows Reaction (3) but not Reactions (4), (5) and (7) giving nitrite/nitrate species, which could be adsorbed on hematite surface and, therefore, the NO<sub>x</sub> removal efficiency results were very poor ( $\approx 6\%$ ). This can be explained on the basis of the photocatalytic properties inherent to hematite. In the case of Fe<sub>2</sub>O<sub>3</sub> (1.9–2.2 eV band gap), the VB and CB are positioned in such a way that the redox potential of the VB hole is sufficient to promote Reaction (2), but the CB electron is not sufficiently negative to generate superoxide radicals in Reaction (6) [69]. Conversely, the characteristic short excited-state lifetime (ca. 1 ps) and small hole-diffusion length (ca. 2–4 nm) of hematite [32] promote fast hole/electron recombination, thus limiting the existence of sufficient hydroxyl radicals to promote Reaction (4).

### 3.3. C-Fe<sub>2</sub>O<sub>3</sub> samples and NO<sub>x</sub> removal

The RFH-A and RFH-B samples, hematite with different carbon contents, were prepared with the aim of enhancing the photocatalytic behaviour of hematite towards the NO conversion. The use of carbon is justified by its NO-adsorption ability [8]. This strategy has previously been reported for the TiO<sub>2</sub> system and using activated carbon (AC) filters. Thus, the NO removal efficiency increased from 83 to 97% when TiO<sub>2</sub> and TiO<sub>2</sub>/AC filters were used, respectively [41]. Fig. 6 shows the efficiency of the photocatalytic process of removing NO<sub>x</sub> gases when RFH samples are used. Despite the fact that the active surface of these samples is lower than that of NH, the NO conversion is higher, with 18% of NO molecules oxidised under irradiation (Fig. 6a and b). More interestingly, the NO<sub>2</sub> release is minimised by increasing the carbon content. Fig. 6c shows a comparison of the NO and NO<sub>x</sub> removal efficiencies for the three samples. Clearly, the PCO efficiency increases with increasing carbon content, and this relationship is more important in the case of NO<sub>x</sub> removal. The RFH-B sample exhibits the best total NO<sub>x</sub> removal efficiency, with a value of 17%, which is three times higher than that obtained with the NH sample. These results can be explained by considering that the presence of carbon facilitates the adsorption of NO molecules, which are then transferred to Fe<sub>2</sub>O<sub>3</sub> and transformed into NO<sub>2</sub> by the just produced h<sup>+</sup> holes prior to hole/electron recombination. The rising number of NO<sub>2</sub> molecules that remain adsorbed on the hematite surface probably have sufficient time to be oxidised to NO<sub>3</sub><sup>-</sup>, following Reaction (4), as suggested by the small NO<sub>2</sub> profile observed for the RFH-B sample during irradiation. Moreover, as reported in previous works concerning to the use of carbon-containing TiO<sub>2</sub> for De-NO<sub>x</sub> applications [70,71], the enhanced photocatalytic behaviour could be also ascribed to the effect of carbonaceous species' structure on reducing the probability of hole/electron recombination.

In the other hand, the preliminary tests to evaluate the deactivation/regeneration of photocatalyst during successive reactions seem to be very promising. In the case of RFH-B sample the tests were performed by executing three additional recycling reactions for the photocatalytic degradation of NO under UV–Vis light irradiation. Between experiments, with the aim to eliminate the nitrite/nitrate compounds accumulated on surface, the sample was washed with distilled water. From Fig. S5 no obvious loss of the photocatalytic activity was observed indicating the good regeneration of RFH-B photocatalyst after each cycle.

The total NO<sub>x</sub> removal efficiency observed for the RFH-B sample (17%) is similar to that reported for other visible-light photocatalysts, InVO<sub>4</sub> and In(OH)<sub>x</sub>S<sub>y</sub> [25,26]; however, the initial rate

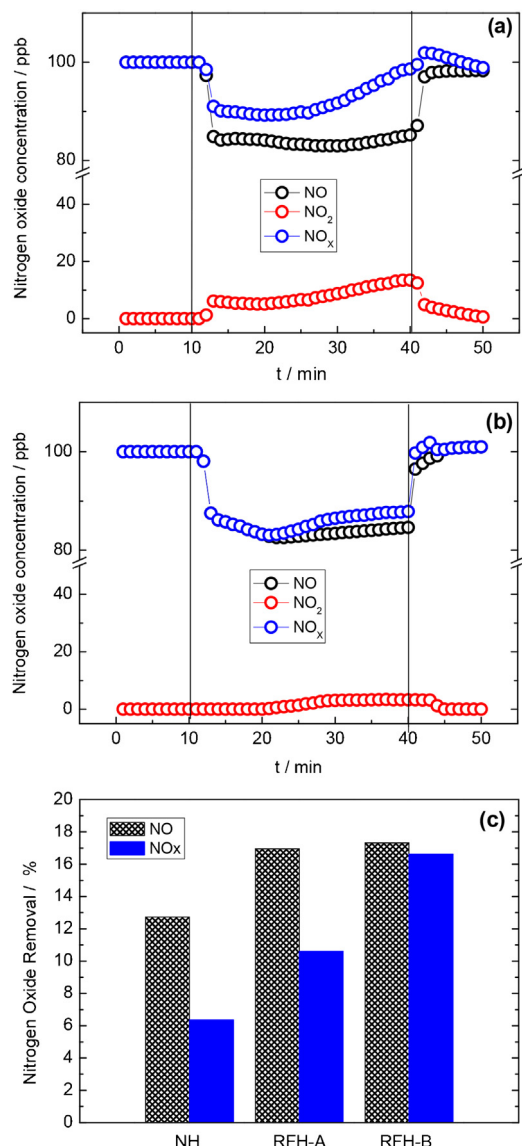


**Fig. 6.** Nitrogen oxide concentration profiles obtained during the photochemical degradation of NO gas, under UV–Vis light irradiation, over (a) RFH-A and (b) RFH-B samples. (c) Nitrogen oxide removal efficiency for the  $\text{Fe}_2\text{O}_3$  samples studied.

constants for  $\text{NO}_x$  degradation are almost two times higher for the hematite samples (Fig. S6), indicating its promising use for air purification. For comparison purpose, the  $\text{TiO}_2$  Evonik-P25 photocatalytic additive was used. Thus, the efficacy of both RFH-B and  $\text{TiO}_2$ -P25 samples to promote the De- $\text{NO}_x$  reaction under visible-light irradiation was studied (Fig. S7). The hematite sample remained active towards the photochemical process whereas the titanium dioxide was inert. Under similar conditions (visible-light irradiation with  $\lambda > 510 \text{ nm}$ ), the  $\text{NO}_x$  removal efficiency of N- and S-doped  $\text{TiO}_2$  systems was around 12% [28,29], and only high and interesting values (>35% PCO efficiency) were obtained through the use of platinum, a very expensive metal, as dopant element [28,31] or by using N-F- as co-dopants [72].

#### 4. Conclusions

In this work, hematite ( $\alpha\text{-Fe}_2\text{O}_3$ ) was proposed as an efficient De- $\text{NO}_x$  photocatalyst. Three samples were studied: NH, RFH-A and RFH-B. The RFH samples were obtained by using resorcinol-formaldehyde as a template and carbon source. The

combined use of XRD, XPS and Raman techniques revealed that all samples contained  $\alpha\text{-Fe}_2\text{O}_3$ , and the presence of other iron oxides or oxyhydroxides phases was discarded. Moreover, the presence of C in the RFH samples was stated by chemical analysis and XPS study, appearing in the amount of 0.9 and 3.5% for RFH-A and RFH-B samples, respectively.

The proposed photochemical oxidation (PCO) mechanism and capture of  $\text{NO}_x$  gases imply the participation of  $\alpha\text{-Fe}_2\text{O}_3$  with atmospheric oxygen, water and UV-A radiation. This mechanism follows the  $\text{NO} \rightarrow \text{NO}_2 \rightarrow \text{NO}_3^-$  photo-oxidation process, from which NO and  $\text{NO}_2$  toxic gases are retained as  $\text{HNO}_2/\text{NO}_3^-$  on hematite particles surface. For the first time, this De- $\text{NO}_x$  mechanism was validated for hematite being the adsorbed products ( $\text{NO}_3^-$ ), which were identified by IR spectroscopy. Nevertheless, the photocatalytic process shows a very low performance in pure hematite (the NH sample), because of the inherently poor photocatalytic properties. However, the efficiency of hematite towards the PCO De- $\text{NO}_x$  process was clearly enhanced in C-hematite compounds. On RFH samples the release of  $\text{NO}_2$  gas, produced during the PCO process, was mitigated and the total  $\text{NO}_x$  removal efficiency was as high as 17%. The presence of C probably assists in the PCO process, owing to its NO-adsorption ability and by reducing the probability of hole/electron recombination.

#### Acknowledgements

This work was funded by Junta de Andalucía (Group FQM-175 and P09-FQM-4764 Project from Consejería de Innovación, Ciencia y Empresa) and the European Union (Programa Operativo FEDER de Andalucía 2007–13).

#### Appendix A. Supplementary data

Supplementary data associated with this article can be found, in the online version, at <http://dx.doi.org/10.1016/j.apcatb.2014.10.025>.

#### References

- [1] M.W. Frampton, I.A. Greaves, Am. J. Respir. Crit. Care Med. 179 (2010) 1077–1078.
- [2] M.L. Williams, D.C. Carslaw, Atmos. Res. 45 (2011) 3911–3912.
- [3] L. Cassar, P. Baglioni, International RILEM Symposium on Photocatalysis, Environment and Construction Materials, RILEM, Florence, 2007.
- [4] J.S. Dalton, P.A. Janes, N.G. Jones, J.A. Nicholson, K.R. Hallam, G.C. Allen, Environ. Pollut. 120 (2002) 415–422.
- [5] S. Devahasdin, C. Fan Jr., K. Li, D.H. Chen, J. Photochem. Photobiol. A 156 (2003) 161–170.
- [6] C.S. Poon, E. Cheung, Constr. Build. Mater. 21 (2007) 1746–1753.
- [7] J. Zhao, X. Yang, Build. Environ. 38 (2003) 645–654.
- [8] C.H. Ao, S.C. Lee, Appl. Catal. B Environ. 44 (2003) 191–205.
- [9] A.G. Kontos, A. Katsanaki, V. Likodimos, T. Maggos, D. Kim, C. Vasilakos, D.D. Dionysiou, P. Schmuki, P. Falaras, Chem. Eng. J. 179 (2012) 151–157.
- [10] A. Folli, S.B. Campbell, J.A. Anderson, D.E. Macphee, J. Photochem. Photobiol. A 220 (2011) 85–93.
- [11] M.M. Ballari, M. Hunger, G. Hüskens, H.J.H. Brouwers, Appl. Catal. B Environ. 95 (2010) 245–254.
- [12] M. Lackhoff, X. Prieto, N. Nestle, F. Dehn, R. Niessner, Appl. Catal. B Environ. 43 (2003) 205–216.
- [13] M.M. Ballari, M. Hunger, G. Hüskens, H.J.H. Brouwers, Catal. Today 151 (2012) 71–76.
- [14] T. Martinez, A. Bertron, E. Ringot, G. Escadeillas, Build. Environ. 46 (2011) 1808–1816.
- [15] M. Hunger, G. Hüskens, H.J.H. Brouwers, Cem. Concr. Res. 40 (2010) 313–320.
- [16] G.L. Guerrini, Constr. Build. Mater. 27 (2012) 165–175.
- [17] R. Sugrañez, J.I. Álvarez, M. Cruz-Yusta, I. Márquez, J. Morales, J. Vila, L. Sánchez, Build. Environ. 69 (2013) 55–63.
- [18] D.T. Gea, Technical Workshop on Depolluting Building Materials Applied to Large Infrastructures, Iberian Association of Photocatalysis, Madrid, 2013.
- [19] H. Chen, Ch.E. Nanayakkara, V.H. Grassian, Chem. Rev. 112 (2012) 5919–5948.
- [20] M. Pelaez, N.T. Nolan, S.C. Pillai, M.K. Seery, P. Falaras, A.G. Kontos, P.S.M. Dunlop, J.W.J. Hamilton, J.A. Byrne, K. O'Shea, M.H. Entezari, D.D. Dionysiou, Appl. Catal. B Environ. 125 (2012) 331–349.

- [21] A. Folli, J.Z. Bloh, M. Strøm, T.P. Madsen, T. Henriksen, D.E. MacPhee, *J. Phys. Chem. Lett.* 5 (2014) 830–832.
- [22] Y. Huang, Z. Ai, W. Ho, M. Chen, S. Lee, *J. Phys. Chem. C* 114 (2010) 6342–6349.
- [23] Z. Ai, W. Ho, S. Lee, L. Zhang, *Environ. Sci. Technol.* 43 (2009) 4143–4150.
- [24] E. Luévano-Hipólito, A. Martínez-de la Cruz, Q.L. Yu, H.J.H. Brouwers, *Appl. Catal. A Gen.* 468 (2013) 322–326.
- [25] Z. Ai, L. Zhang, S. Lee, *J. Phys. Chem. C* 114 (2010) 18594–18600.
- [26] S. Ge, L. Zhang, *Environ. Sci. Technol.* 45 (2011) 3027–3033.
- [27] H. Li, S. Yin, Y. Wang, T. Sato, *J. Am. Ceram. Soc.* 96 (2013) 1258–1262.
- [28] S. Yin, B. Liu, P. Zhang, T. Morikawa, K. Yamanaka, T. Sato, *J. Phys. Chem. C* 112 (2008) 12425–12431.
- [29] N. Todorova, T. Vaimakis, D. Petrakis, S. Hishita, N. Boukos, T. Giannakopoulou, M. Giannouri, S. Antiohos, D. Papageorgiou, E. Chaniotakis, C. Trapalis, *Catal. Today* 209 (2013) 41–46.
- [30] D. Zhang, M. Wen, S. Zhang, P. Liu, W. Zhu, G. Li, H. Li, *Appl. Catal. B Environ.* 147 (2014) 610–616.
- [31] C.-H. Huang, I. Wang, Y. Lin, Y. Tseng, Ch. Lu, *J. Mol. Catal. A Chem.* 316 (2010) 163–170.
- [32] D.A. Wheeler, G. Wang, Y. Ling, Y. Li, Z. Zhang, *Energy Environ. Sci.* 5 (2012) 6682–6702.
- [33] H. Xie, Y. Li, S. Jin, J. Han, X. Zhao, *J. Phys. Chem. C* 114 (2010) 9706–9712.
- [34] Y. Shi, H. Li, L. Wang, W. Shen, H. Chen, *ACS Appl. Mater. Interfaces* 4 (2012) 4800–4806.
- [35] W. Sun, Q. Meng, L. Jing, D. Liu, Y. Cao, *J. Phys. Chem. C* 117 (2013) 1358–1365.
- [36] D. Barreca, G. Carraro, A. Gasparatto, Ch. Maccato, F. Rossi, G. Salvati, M. Talarida, Ch. Das, F. Fresno, D. Korte, U. Lavrencic, M. Franko, D. Schmeisser, *ACS Appl. Mater. Interfaces* 5 (2013) 7130–7138.
- [37] R. Sugráñez, M. Cruz-Yusta, I. Mármol, J. Morales, L. Sánchez, *ChemSusChem* 6 (2013) 2340–2347.
- [38] G. Carraro, R. Sugráñez, C. Maccato, A. Gasparotto, D. Barreca, C. Sada, M. Cruz-Yusta, L. Sánchez, *Thin Solid Films* 564 (2014) 121–127.
- [39] H.U. Lee, G. Lee, J.C. Park, Y.-C. Lee, S.M. Lee, B. Son, S.Y. Park, C. Kim, S. Lee, S.C. Lee, B. Nam, J.W. Lee, D.R. Rae, J.-S. Yoon, J. Lee. 2014, *Chemical Engineering Journal* 240:91–98.
- [40] M.-Q. Yang, N. Zhang, Y.-J. Xu, *Appl. Mater. Interfaces* 5 (2013) 1156–1164.
- [41] C.H. Ao, S.C. Lee, *Chem. Eng. Sci.* 60 (2005) 103–109.
- [42] R.M. Cornell, U. Schwertmann (Eds.), *The Iron Oxides: Structure, Properties, Reactions, Occurrences and Uses*, 2nd edn., Wiley-VCH Verlag GmbH & Co. KGaA, 2003, p. 382.
- [43] J. Chen, Y.-C. Zou, F. Zhang, Y.-C. Zhang, F.-F. Guo, G.-D. Li, *J. Alloys Compd.* 563 (2013) 264–268.
- [44] J.-W. Wen, D.-W. Zhang, Y. Zang, X. Sun, B. Cheng, C.-X. Ding, Y. Yu, C.-H. Chen, *Electrochim. Acta* 133 (2014) 515–521.
- [45] D. Fujikawa, M. Uota, T. Yoshimura, G. Sakai, T. Kijima, *Chem. Lett.* 35 (2006) 432–433.
- [46] T. Yamashita, P. Hayes, *Appl. Surf. Sci.* 254 (2008) 2441–2449.
- [47] ISO 22197-1, “Fine Ceramics (Advanced Ceramics, Advanced Technical Ceramics) – Test Method for Air Purification Performance of Semiconducting Photocatalytic Materials – Part 1: Removal of nitric oxide”, 2007.
- [48] W. Ruland, in: P.L. Walker (Ed.), *Chemistry and Physics of Carbon*, Marcel Dekker, New York, 1968, pp. 1–84.
- [49] G.K. Pradhan, K.M. Parida, *Appl. Mater. Interfaces* 3 (2011) 317–323.
- [50] T.-C. Lin, G. Seshadri, J.A. Kelber, *Appl. Surf. Sci.* 119 (1997) 83–92.
- [51] J. Morales, L. Sánchez, F. Martín, F. Berry, X. Ren, *J. Electrochem. Soc.* 159 (2005) A1748–A1754.
- [52] R.S. Schrebler, L. Ballesteros, A. Burgos, E.C. Muñoz, P. Grez, D. Leinen, F. Martín, J.R. Ramos-Barrado, E.A. Dalchiele, *J. Electrochem. Soc.* 158 (2011) D500–D505.
- [53] N. Muhler, R. Schlögl, G. Ertl, *J. Catal.* 138 (1992) 413–444.
- [54] D.D. Hawn, B.N. DeKoven, *Surf. Interface Anal.* 10 (1987) 63–74.
- [55] G. Riveros, D. Ramírez, E.A. Dalchiele, R. Marotti, P. Grez, F. Martín, J.R. Ramos-Barrado, *J. Electrochem. Soc.* 161 (2014) D353–D361.
- [56] I. Cesar, K. Sivula, A. Kay, R. Zboril, M. Grätzel, *J. Phys. Chem. C* 113 (2009) 772–782.
- [57] D. Bersani, P.P. Lottici, A. Montenero, *J. Raman Spectrosc.* 30 (1999) 355–360.
- [58] A.A. Tahir, K.G.U. Wijayantha, S. Saremi-Yarahmadi, M. Mazhar, V. McKee, *Chem. Mater.* 21 (2009) 3763–3772.
- [59] P. Lottici, C. Baratto, D. Bersani, G. Antonioli, A. Montenero, M. Guarneri, *Opt. Mater.* 9 (1998) 368–372.
- [60] I. Mármol, P. Ballester, S. Cerro, G. Monrós, J. Morales, L. Sánchez, *Cem. Compos.* 32 (2010) 617–622.
- [61] A.B. Lever, *Studies in Physical and Theoretical Chemistry Inorganic Electronic Spectroscopy*, Elsevier, Amsterdam, 1986.
- [62] M. Niu, F. Huang, L. Cui, P. Huang, Y. Yu, Y. Wang, *ACS Nano* 4 (2010) 681–688.
- [63] B.Y. Yu, S.Y. Kwak, *J. Mater. Chem.* 22 (2012) 8345–8353.
- [64] S. Banerjee, S.C. Pillai, P. Falaras, K.E. O’Shea, J.A. Byrne, D.D. Dionysiou, *J. Phys. Chem. Lett.* 5 (2014) 2543–2554.
- [65] T. Ibusuki, in: M. Kaneko, I. Okura (Eds.), *Photocatalysis. Science and Technology*, Springer, New York, 2002, pp. 143–155.
- [66] F.A. Miller, C.H.H. Wilkins, *Anal. Chem.* 24 (1952) 1253–1294.
- [67] Q. Wu, Ch. Yang, R. Van de Krol, *Catal. Today* 225 (2014) 96–101.
- [68] R.S. Wade, C.E. Castro, *Chem. Res. Toxicol.* 9 (1996) 1382.
- [69] R. Vinu, G. Madras, *J. Indian Inst. Sci.* 90 (2010) 189–230.
- [70] Y.-H. Tseng, C.-H. Kuo, *Catal. Today* 174 (2011) 114–120.
- [71] Y. Huang, W. Ho, S. Lee, L. Zhang, G. Li, J.C. Yu, *Langmuir* 24 (2008) 3510–3516.
- [72] A.V. Katsanaki, A.G. Kontos, T. Maggos, M. Pelaez, V. Likodimos, E.A. Pavlatou, D.D. Dionysiou, P. Falaras, *Appl. Catal. B Environ.* 140–141 (2013) 619–625.